NANO · MICRO small
www.small-journal.com

Strategies for Constructing and Operating DNA Origami Linear Actuators

Erik Benson, Rafael Carrascosa Marzo, Jonathan Bath, and Andrew J. Turberfield**

Linear actuators are ubiquitous components at all scales of engineering. DNA nanotechnology offers a unique opportunity for bottom-up assembly at the molecular scale, providing nanoscale precision with multiple methods for constructing and operating devices. In this paper, DNA origami linear actuators with up to 200 nm travel, based on a rail threading a topologically locked slider, are demonstrated. Two strategies, one- and two-pot assembly, are demonstrated whereby the two components are folded from one or two DNA scaffold strands, respectively. In order to control the position of the slider on the rail, the rail and the inside of the slider are decorated with single-stranded oligonucleotides with distinct sequences. Two positioning strategies, based on diffusion and capture of signaling strands, are used to link the slider reversibly to determined positions on the rail with high yield and precision. These machine components provide a basis for applications in molecular machinery and nanoscale manufacture including programmed chemical synthesis.

1. Introduction

In the last few decades, DNA nanotechnology has progressed from conjecture[1] to widespread implementation.[2] DNA nanotechnology includes dynamic devices, in which strand-displacement reactions are used for detection,[3] computation,[4] actuation,[5–9], control of chemical reactions,[10,11] and structural nanotechnology, where DNA is used as a construction material. The development of structural DNA nanotechnology was accelerated by the introduction of DNA origami,[12,13] whereby a long scaffold strand is folded by annealing with hundreds of short staple strands to create complex designs with high precision and yield. DNA origami has been applied to biophysical studies,[14–17] proof-of-concept devices for therapeutics[5,18,19] and manufacturing,[20–22] and to template plasmonic and electronic devices.[23,24] DNA origami has also been used to create nanoscale mechanical components, including switchable containers,[5,6,25] rotor arms,[26–28] and sliders.[29–32]

Linear actuators are indispensable mechanical components, used in mechanisms on all scales from hydraulic cylinders in construction machinery to piezoelectric elements for nanometer-scale manipulation. In this paper, we use DNA origami to construct linear actuators consisting of a rail with a topologically locked slider. We use addressable DNA linkers, reconfigurable through strand-displacement reactions, to reversibly lock the slider in pre-determined positions along the rail.

The first synthetic DNA rotaxane[32] consisted of slider, stoppers, and rail created from double-stranded DNA. Slider position has been controlled using DNA control strands,[32] pH,[33] and light,[34] and coupled to a catalytic output.[35] The first DNA slider mechanism constructed from multiple parallel helices using the origami technique, enabling greater travel and rigidity, was demonstrated by Marras et al.[29]: slider and rail were constructed together using a single scaffold strand of which four sections were left as flexible, single-stranded DNA (ssDNA) links between slider and rail. The mechanism showed free linear diffusive motion of the slider along the rail but the ssDNA links constrained its rotary motion. Later, it was demonstrated that slider and rail could be assembled as separate DNA origami structures, then combined either by closing the slider around the rail[30] or by threading a two-part rail[31] through the slider to create a rotaxane with free linear and rotary motion. These two strategies – assembly of rail and slider from a single scaffold in a one-pot reaction or, separately, as distinct DNA origami structures – have their own advantages and disadvantages. The size of a DNA origami nanostructure is limited by the length of the scaffold strand: a device made in a one-pot assembly reaction has, in general, less DNA available for construction than a two-pot device comprising two scaffold strands. One-pot assembly is a simpler process but may be more difficult to tune than two-pot assembly in which the two structures are folded and purified independently. The loading of slider onto rail creates interesting constraints. In a one-pot system, the connections formed between slider and rail by the scaffold ensures that the two components interact at high effective local concentration, independent of the global origami concentration; in a two-pot reaction scheme, the assembly rate depends on the absolute concentrations of the DNA origami components which are typically much lower, leading to slower interaction rates. In one-pot assembly, the

Dr. E. Benson, R. Carrascosa Marzo, Dr. J. Bath, Prof. A. J. Turberfield
Department of Physics
University of Oxford
Parks Road, Oxford OX1 3PU, UK
E-mail: erik.benson@physics.ox.ac.uk;
andrew.turberfield@physics.ox.ac.uk

The ORCID identification number(s) for the author(s) of this article can be found under https://doi.org/10.1002/smll.202007704.

DOI: 10.1002/smll.202007704

slider and rail necessarily assemble in a perfect 1:1 ratio; when combining separately-assembled components, it may be necessary to add one of them in excess to drive the assembly reaction to near-completion. In this paper, we explore these questions by creating DNA origami linear actuators with similar architectures using both one- and two-pot assembly strategies.

2. Results

In a one-pot assembly scheme, in which both slider and rail are folded from the same scaffold strand, the slider and rail are connected by at least one scaffold linkage (two for a circular scaffold) after assembly. In order to achieve free motion of the rotaxane, these tethers could either be designed to be sufficiently long and flexible that they do not significantly hinder sliding or cut by restriction enzymes after assembly. The scaffold-tether strategy is limited by the need to use precious scaffold material on the tethers and the risk that secondary structure in the tethers limits their length and flexibility. We pursued a restriction enzyme route, using the enzyme BstYI that cuts the commonly-used M13-derived scaffold p8064 twice to create one short (1498 nt) and one long (6566 nt) fragment, suitable for post-assembly division into slider and rail respectively. Alternative ways to cut single-stranded links within DNA origami include use of self-cleaving DNAzymes[36] or RNA-guided endonucleases.[37] In our alternative two-pot assembly, we used a standard-size scaffold (p8064) to create the rail and a shorter phagemid-based[38] scaffold (2880 nt) to create the slider. In both strategies, we chose to base the rail on a six-helix-bundle honeycomb design, offering a reasonable compromise between material use and rigidity: previous studies[39–41] indicate that this design has a persistence length above 1 μm. For this study, we made the rail as long as possible in order to simplify determination of the slider position by microscopy; the rail could be redesigned with a larger cross-section and shorter length to increase rigidity. Both architectures incorporated triangular stopper blocks at the ends of the rail to prevent the slider from unthreading. The lengths of the rail between stoppers were ≈205 and 220 nm for the one- and two-pot structures, respectively.

The sliders were designed to be a close fit but still capable of diffusing freely along the rail. We assessed prototype designs using the coarse-grained DNA simulation package oxDNA[42] with a short, six-helix-bundle rail and short sliders comprising 14–20 helices: all were predicted to be capable of diffusion along the slider (Figure S1, Supporting Information). For the one-pot assembly, we based the slider on an approximately circular single-layer, 18-helix, architecture to allow enough space for attachment sites between the rail and the inside of the slider. For the two-pot system, where more material was available for incorporation in the slider, we used a pleated single-layer, 30-helix design. In both cases, the scaffold strand did not encircle the rail, rather, the slider incorporated a seam at which, by omitting staple strands, it could be opened to allow the rail to pass through (Figures S2–S6, Supporting Information).

2.1. Assembly and Purification

Analysis by agarose gel electrophoresis (Figure S7, Supporting Information) indicated that both structures folded well. Both were imaged by negative-stain transmission electron microscopy (TEM) (**Figure 1**).

The one-pot structure was designed such that it could fold directly in the rotaxane configuration with the rail threading the slider. However, electron micrographs showed that many sliders closed outside the rail (Figure S8, Supporting Information). To overcome this, we omitted two sets of staple strands during the first stage of assembly: the seam staples needed to close the slider around the rail; and a row of "hinge staples" on the opposite side of the slider to provide flexibility, enabling a gap

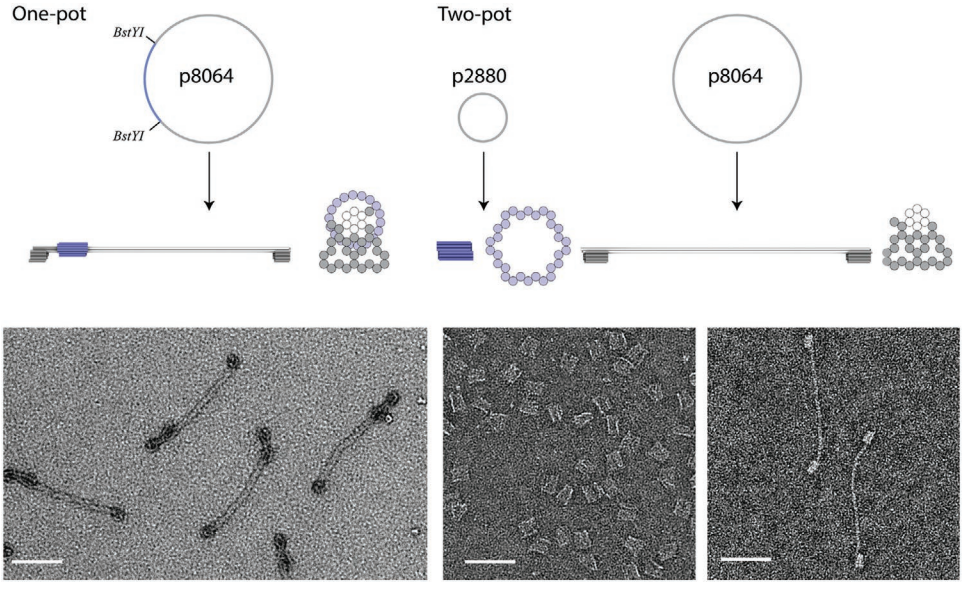

Figure 1. Construction of slider rail devices from one or two scaffold strands. Top: overview of one-pot and two-pot assembly scheme, with top and side renders of slider and rail, based on cadnano designs. Bottom: TEM images of assembled structures, scale bars 100 nm.

to open at the seam. To drive assembly of the slider on the rail, we added eight single-stranded staple extensions, protruding from the inside of the slider, and eight complementary staple extensions protruding from the rail (Figure S6, Supporting Information). Seam and hinge staples were added after folding. After assembly, we broke the connection between slider and rail by a combination of strand displacement (to break the templating links between staples in slider and rail) and restriction enzyme digestion of the two scaffold regions bridging the slider and rail, achieving a device yield (rails threading sliders) of 30% as determined by TEM (Figure S9, Supporting Information). To further enhance the yield of correctly assembled rotaxanes, we employed a magnetic bead purification strategy[43]. A poly-adenosine tail was attached to the slider as an extension to a staple strand. After slider separation, samples were mixed with poly-thymidine magnetic beads to bind correctly-assembled devices consisting of sliders and rails, also free sliders. The beads were washed to remove rails lacking sliders as well as restriction enzymes: strand-displacement was then used to release the devices from the beads. This doubled the proportion of rails threading sliders to 61% (Figure S10, Supporting Information). Unconnected sliders, also enriched by this procedure, were removed when devices were immobilized on glass surfaces for visualization experiments as described below.

For the two-pot system, the rail and the slider were folded in separate reactions then purified from excess staple strands using polyethylene glycol (PEG) precipitation. The two components were then mixed at a 1:1 ratio and incubated for three days at 37 °C. After gel extraction, the proportion of correctly assembled rotaxanes was determined to be 44% by TEM (Figure S11, Supporting Information).

We used a Python image-processing pipeline to track the positions of sliders observed in electron micrographs. For the free rotaxane structure, we observed a uniform distribution of the slider along the rail indicating that the sliders are free to move with no preferred position along the rail (**Figure 2;** and Figure S12, Supporting Information).

To study the motion of the slider along the rail, we used DNA–PAINT super-resolution microscopy.[44] By functionalizing one surface of each stopper with biotin we immobilized the assembled actuators, by addition of bridging molecules of streptavidin, on a glass coverslip functionalized with a layer of biotinylated bovine serum albumin. By labeling the stoppers and the slider with orthogonal DNA–PAINT handle sequences, we were able to separately image slider and rail using exchange-PAINT.[45] In approximately 53% of immobilized devices, we were able to observe diffusive motion of the slider along the rail (Figure 2E). We also used DNA–PAINT to study the one-pot device with the slider immobilized in the middle of the track (Figure S13, Supporting Information).

2.2. Controlled Positioning

In order to control the position of the slider on the rail, we developed two strategies based on reversible connections between single-stranded linker oligonucleotides (extended staples) protruding from the inside of the slider and others forming an addressable track along the rail (**Figure 3**). In the first strategy, which we call "non-interacting addresses", linkers are 12 nt long and are taken from a set designed to be orthogonal (i.e., to cross-hybridize weakly, if at all, with other members of the set or their reverse complements). Two linkers inside the slider and a double row of "address" linkers on the rail are used for positioning: to bind the slider in a specific position the linkers on the slider are connected to a corresponding pair of "address" linkers using specific bridge oligonucleotides. The bridge oligonucleotides incorporate a toehold region at one end, enabling the linkage between slider and rail to be undone through the addition of specific release strands that compete for binding to the bridges.[46] In the second strategy, which we call "interacting addresses", for each docking position there is a set of four address linkers on the inside of the slider that are complementary to corresponding address linkers on the rail. Removable blocking strands, which bind to the linkers on the rail, are used to ensure that only one position on the rail is available for slider binding. We chose to use non-interacting addresses in the one-pot system and interacting addresses in the two-pot system because the two-pot slider is larger and can accommodate many address linkers. We used TEM to test whether sliders could be moved to five different positions for the non-interacting address system and to three positions for the interacting address system. The polarities of the structures are not distinguishable by TEM but were inferred from the measured slider positions. Using both methods, we were able to control the position of the slider on the rail in good agreement with the design (Figure 3C; and Figures S14–S29, Supporting Information). When we added release strands to complete a stepping cycle, TEM imaging confirmed that released sliders were returned to a freely diffusing state in high yield (Figure 3E).

The positioning accuracy of the systems demonstrated here is limited by thermal fluctuations. To estimate the magnitude of this effect, we used oxDNA to simulate the actuators with sliders locked in a central position. From the simulation trajectory, we tracked the distance between the slider and two reference points, defined as the centres of mass of clusters of six bases within the rail. One reference point (proximal) is located within the tethered slider and one (distal) is located next to a stopper (**Figure 4**). The proximal point was chosen to study fluctuations in the position of the slider relative to the rail, whereas the distance to the distal point also depends on fluctuations in the rail segment between the slider and the stopper. For the one-pot system, the fluctuations in distance were mostly less than ±1 nm for the proximal and ±2 nm for the distal point. Occasional larger fluctuations of up to 6 nm were observed. The two-pot device showed a different behavior with larger, slower fluctuations in distance which are associated with fluctuations in the shape of the much larger slider structure. For both devices, the fluctuations in distance to the distal point were only marginally larger than fluctuations relative to the proximal point indicating that, at this scale, the inherent flexibility of the slider itself and of the links to the rail dominate the precision of slider positioning.

3. Discussion

One-pot assembly was significantly faster than two-pot assembly and completed in hours instead of days: it has the

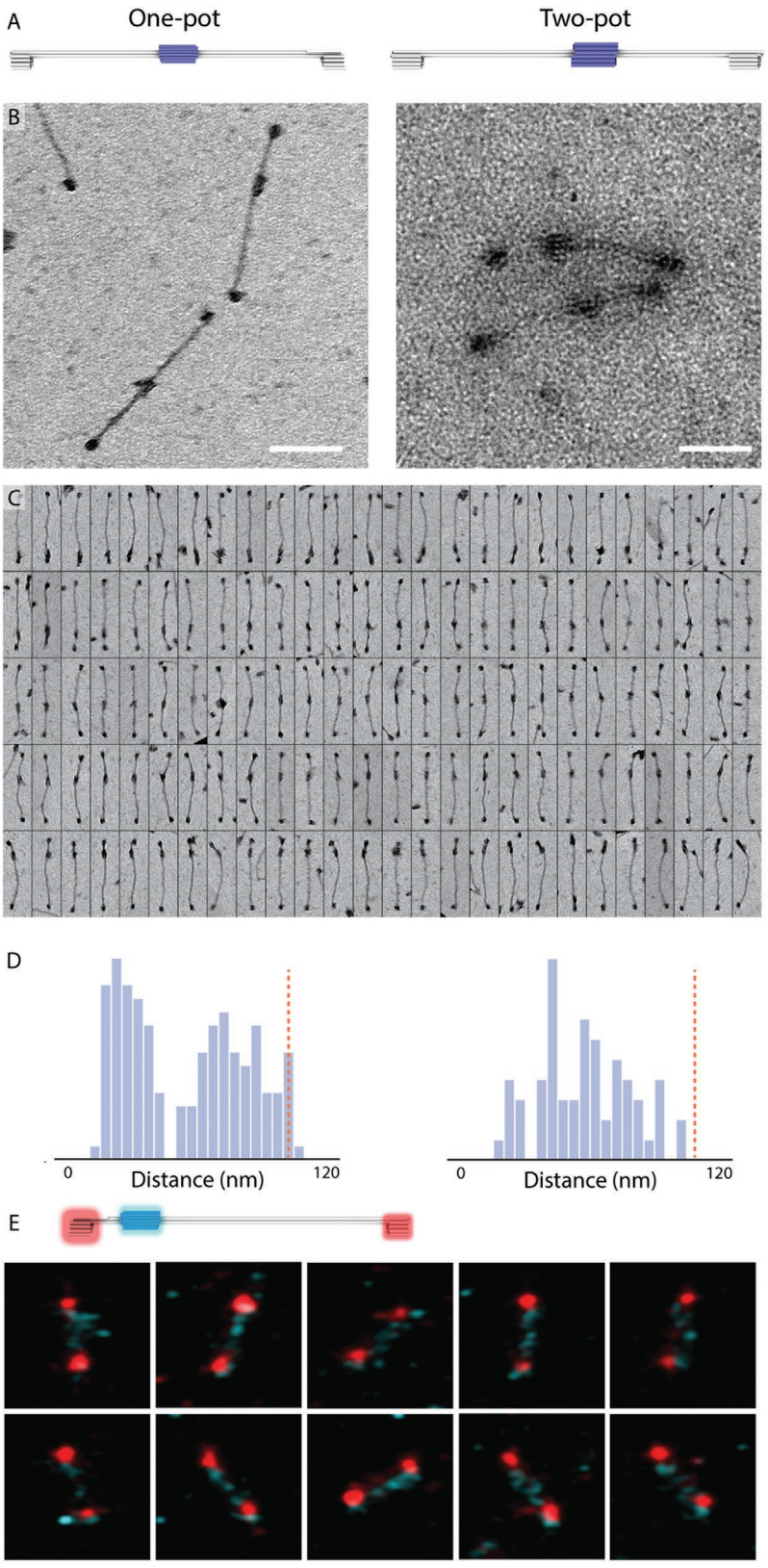

Figure 2. Assembly of the linear actuators and diffusive motion of slider on rail. A) rendering and B) TEM images of the one-pot and two-pot devices with the slider freely diffusing, scale bars 100 nm. C) TEM images of one-pot device with freely diffusing slider; images are sorted by position of slider and cropped in 100 × 300 nm boxes. D) Distribution of distance from the slider center to the closest end of the rail for one-pot (left) and two-pot (right) devices. Dotted lines indicate distances to the mid-point of the rail. E) DNA–PAINT super-resolution micrographs of the freely moving slider (blue) and the stoppers (red) of the one-pot device, cropped in 500 nm boxes.

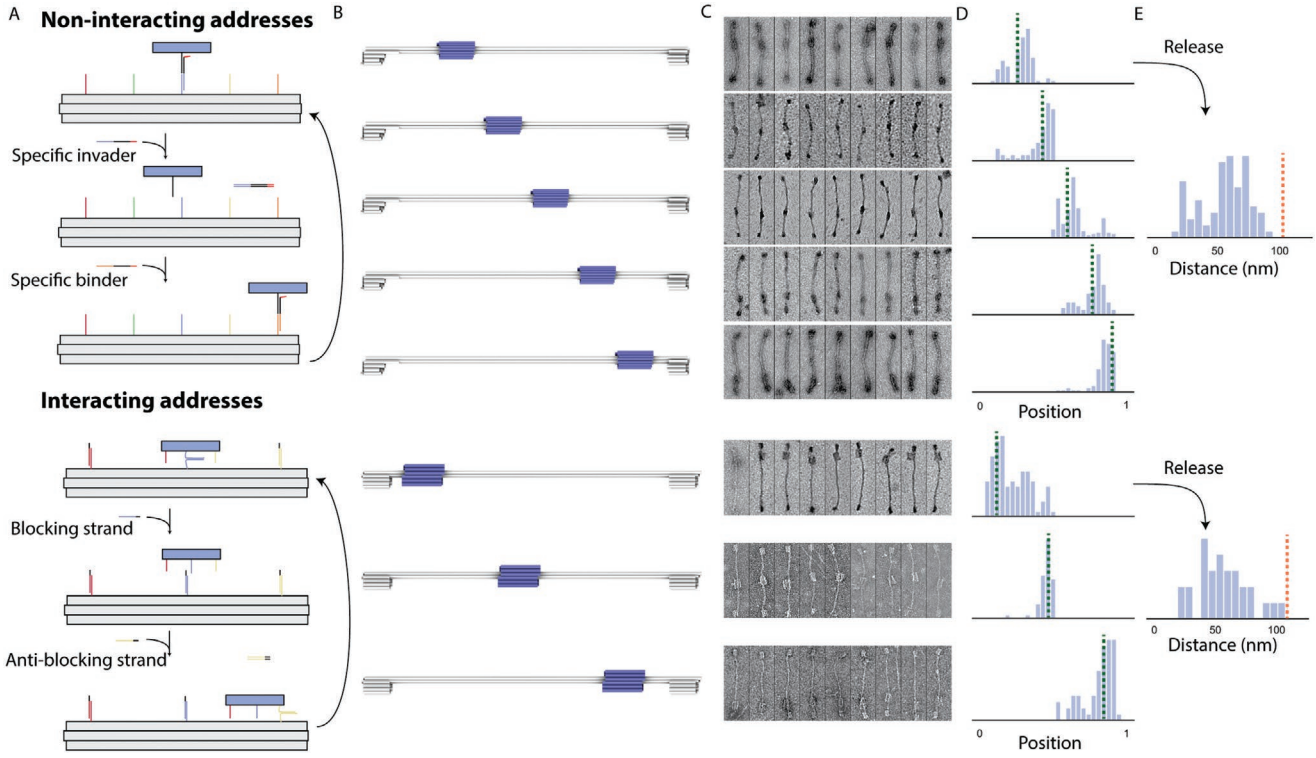

Figure 3. Controlling the position of the linear actuators. A) Schematic of the two systems for reversibly binding the slider to a specific position on the rail. The number of linker duplexes used to bind the slider at each position is two with non-interacting addresses (one-pot device) and four with interacting addresses (two-pot device). B) The non-interacting and interacting addresses were used to drive the slider of the one-pot device to five pre-defined positions and the two-pot device to three positions. C) TEM images of the actuators locked in position, cropped in 100 × 300 nm boxes. D) Distribution of slider positions (normalized to rail length) for devices locked in different positions; dotted line indicates designed position. E) Distribution of distance from slider to closest end for devices released to freely diffusing state after being locked. Dotted lines indicate distances to the mid-point of the rail.

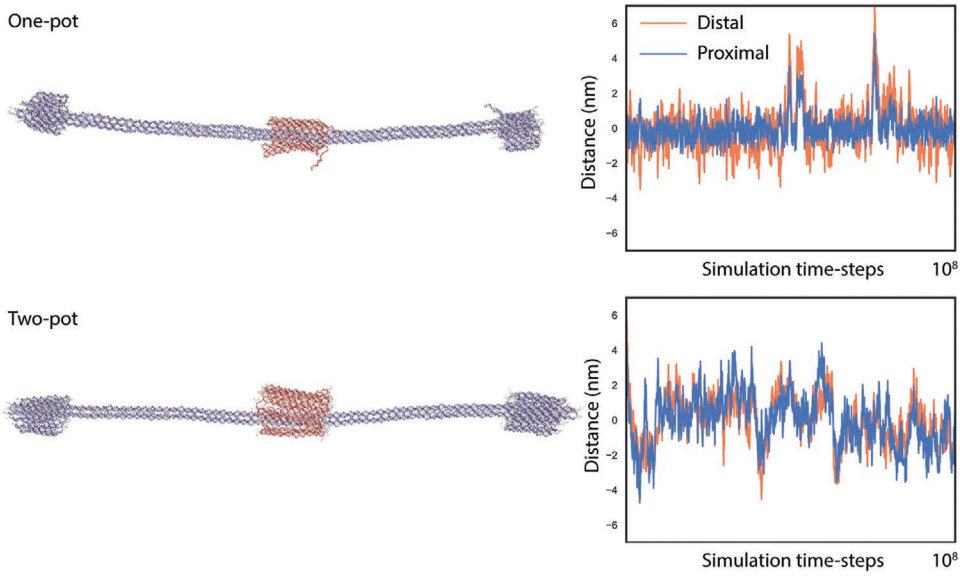

Figure 4. Study of actuator precision for one- and two-pot devices, with 18- and 31-helix sliders respectively, by oxDNA. The origami structures were prepared locked into their most central binding site and simulated for 10^8 time steps. The images show the final configurations. Fluctuations in slider position were quantified by calculating the distance from the slider to a point on the rail directly inside the slider (proximal) and to a point at the end of the track near a stopper (distal). Deviations from the mean distances are shown.

advantage of high local concentration of interacting components. The design of the one-pot device required careful planning of scaffold sequence placement and the locations of the restriction sites used to separate slider from rail; the two-pot approach is easier to generalize as it is more modular. Closing of the slider around the rail and its subsequent release to form a rotaxane is the most significant obstacle to achieving a high device yield. For the one-pot device it is possible that a larger slider diameter would increase the yield of closed devices at the cost of more material used for the slider. The design of the seam region is likely to affect closing yield: further experimentation with increasingly staggered seams and altered closing strand designs may increase yield.

Both systems of signaling strands used to control the actuator configuration are capable of reversibly positioning the slider on the rail with high yield. The interacting-address approach uses blocking and release strands that each need only interact with one address along the rail, with the result that the design of these DNA sequences is more straightforward than that for the non-interacting-address system in which signaling strands incorporate domains complementary to address strands on both slider and rail. The interacting address approach requires a separate set of address strands within the slider for each possible position along the rail, requiring a larger slider. Given the limited length of the scaffold used here, this is easier to implement in combination with the two-pot assembly strategy.

Coarse-grained molecular dynamics simulation was used to study the precision of the systems. When locked in position, the slider position fluctuates within a few nanometers with respect to the rail ends. The rails used here were designed to be as long as possible to exaggerate motion and aid experimental characterization; a system with thicker and thus more rigid rails could enable even higher precision.

4. Conclusion

We have demonstrated the use of DNA origami to create nanometer-scale linear actuators comprising sliders topologically locked to linear rails. We have compared two assembly strategies: one-pot assembly, where both slider and rail are formed from the same scaffold strand; and two-pot assembly, where the slider and rail are folded as independent origamis and then combined to form the final structure. TEM and DNA–PAINT microscopy of devices immobilized on a surface confirmed that both methods can be used to create freely-moving devices.

Linear actuators are crucial components in engineered mechanisms on all length scales. The assembly yield and positioning accuracy that we have demonstrated encourage further development of nanoscale machinery incorporating modular linear actuators. Piezoelectric actuators can achieve comparable or greater precision, but these are macroscopic devices – even in the pilot experiments presented here, we have observed the simultaneous operation of 10^5 molecular devices per mm^2 on a surface, and it would be straightforward to scale up by many orders of magnitude for devices operating in solution. The result of applying such manipulators to the task of programmable assembly would be somewhere between a semiconductor fabrication plant and a chemical reaction. However far-fetched this vision may seem, the economies of cost and scale compared to traditional fabrication methods make the dream of programmable molecular manufacture well worth pursuing.

5. Experimental Section

DNA Origami Design: DNA origami structures were designed using CaDNAno.[47] For the one-pot design, the positioning of the sequence of the p8064 scaffold strand was controlled such that the restriction sites for BstYI occurred on regions linking the slider to the rail.

oxDNA Modeling: DNA origami design files were converted to the oxDNA format using the tacoxDNA web converter.[48] Files were prepared for simulation using editor features in oxView[49] to merge the separate design files for the two-pot slider and rail and to position the slider on the rail for both systems. oxView[49] was also used to initialize the staple–staple interactions used in simulations of the slider locked in position on the rail. Systems were simulated with oxDNA 2.4 using the oxDNA 2 model. The systems were first relaxed in two steps, first with simulation type "min" for ≈5000 time-steps, then by a molecular dynamics simulation with maximum backbone force set to 50 for 10^6 time-steps. The main simulation was run at 20 °C, 0.5 M NaCl, for 10^8 time-steps, with a configuration saved every 50 000 time-steps. Simulation files were visualized in oxView.[49] For the calculation of the distance from the slider to positions on the rail, one nucleotide per helix in the centre of the slider (18 helices for one-pot, and 30 for two-pot) was selected to define the slider position, and one nucleotide per helix of the rail (6 helices) was selected to define both proximal and distal reference positions within the rail. Coordinates for each set of nucleotides were averaged in each saved simulation time-step.

p2880 Scaffold Preparation: p2880 (pJB103) is a 2880 bp phagemid derived from pUC118[50] (sequence in Note S1, Supporting Information). To prepare single-stranded DNA, DH5α was transformed with p2880 and the helper plasmid pSB4423[38] and plated on LB agar containing 100 μg mL^{-1} ampicillin and 33 μg mL^{-1} chloramphenicol. A single colony was transferred to 100 mL of LB supplemented with the same antibiotics and grown with shaking overnight at 37 °C. Cells were removed by centrifugation at 10 000 rpm for 15 min at 4 °C, then, phage was precipitated by adding 1/2 volume of 2.5 M NaCl + 20% PEG-8000 and incubated for 1 h at 4 °C while stirring. Phage were recovered by centrifugation at 10 000 rpm for 15 min at 4 °C, resuspended in 2 mL of TE + 150 mM NaCl, then split into 1 mL aliquots in microcentrifuge tubes. Phage were precipitated a second time by adding 1/10 volume of 2.5 M NaCl + 20% PEG-8000, then, after 5 min at room temperature, pelleted by centrifugation at 13 000 rpm at room temperature in a microfuge. The phage pellet was resuspended in 300 μL of TE then extracted once with phenol, twice with phenol chloroform, and once with chloroform, precipitated with ethanol then resuspended in 100 μL of TE, typically giving a concentration of 1 μM and a yield of about 1 μg per mL of culture.

Origami Assembly: Staple strands were purchased from Integrated DNA Technologies (Tables S1–S3, Supporting Information). Structures were annealed using a thermal ramp, starting with a 5 min incubation at 80 °C followed by rapid cooling from 80 °C to 60 °C over 20 min, then slower cooling from 60 °C to 20 °C over 14 h.

The one-pot system was assembled in a 40 μL volume using 10 nM origami scaffold (p8064, derived from M13 bacteriophage (tilibit nanosystems GmbH, Munich, Germany)) and an excess of 50 nM staple strands in 22 mM $MgCl_2$, 1 × TE (10 mM Tris-HCl containing 1mM EDTA•Na_2) and 50 mM NaCl. Structures were initially assembled without hinge staples or the staples that close the seam of the slider around the rail. After assembly, samples were allowed to equilibrate for a few minutes at 37 °C, then a 2 × excess of seam staples was added (0.8 μL of 1 μM seam mix) and the samples incubated for 1 h to close the seam. After this, 4 μL of 500 nM hinge region staples were added, and the mixture incubated for a further 30 min. Still in the heat block, the samples were then diluted with 38.5 μL of 1 × TE, 50 mM NaCl to reduce the $MgCl_2$ concentration to 12 mM. 3 μL of BstYI enzyme

(10 000 units per mL, New England Biolabs) and 6 µL release strands (12.5 mM each) were added and the samples incubated for a further 1h to separate the slider from the rail.

The rail and the slider of the two-pot system were both assembled using 10 nM origami scaffold (p8064 for the rail and p2880 for the slider), an excess of 100 nM staple mix, 14 mM, and 10 mM $MgCl_2$, respectively, and a buffer comprising 5 mM Tris-HCl, 1 mM EDTA.

The one-pot system structure was purified using magnetic beads. 300 µL of poly-T Dynabead magnetic beads (Thermo Fisher) was transferred to a 1.5 mL tube and put on a magnetic rack. The storage buffer supernatant was removed and the beads resuspended in 80 µL of DNA origami buffer (1 × TE, 10 mM $MgCl_2$, 50 mM NaCl). 20 µL of this concentrated suspension was added to the digested one-pot DNA origami solution and incubated on a rotary mixer at room temperature overnight. Beads were separated and washed three times with 500 µL DNA origami buffer and finally resuspended in 50 µL of DNA origami buffer. 2 µL of 100 µM release invader strands were added and the sample incubated for 2 h on a rotary mixer. Using the magnetic rack, the displaced, purified sample was removed from the beads.

The components of the two-pot system were separately purified by PEG precipitation. An equal volume of 15% PEG 8000 solution (500 mM NaCl, 12.5 mM $MgCl_2$, 1 × TAE) was added to the assembled origami and centrifuged for 30 min at 20 000 g. The supernatant was removed, and the pellet resuspended in the assembly buffer mix. The procedure was repeated three times.

Agarose Gel Electrophoresis: Agarose gel electrophoresis was used for the characterization of the one-pot system structure (2% agarose, 1× TAE with 10 mM $MgCl_2$), and the two-pot system structures (2% agarose, 1× TBE with 12 mM $MgCl_2$), for 3h at 70 V in an ice bath. The apparatus used was the PowerPac Basic Power Supply and Wide Mini-Sub Cell GT from Bio-Rad

Loading of the Slider in Two-Pot System: The loading of the slider on the rail for the two-pot system was done in three sequential incubations. First, a 1:1 mix of the rail and slider was incubated at 37 °C for 3 days. The rail was then incubated for 40 min at RT with an excess of 1 µM blocking strands for two of the three positions in order to block and remove the sliders from all but one attaching point on the rail. The remaining slider was then closed by addition of an excess of 100 nM of closing strands and incubation for 2 h at 35 °C. After closing, the slider was released to a freely moving state through the introduction of a 1 µM excess of blocking strands for the position where the slider was loaded on the rail. The blocking strands remove the attached slider via toehold mediated strand displacement by a 40 min incubation at room temperature. The origami structure loaded with the closed and released slider was gel-extracted using the same agarose gel conditions but with a 1% agarose gel.

Slider Positioning: For interacting-address positioning in the two-pot system, the gel-extracted structures were incubated with an excess of 50 nM of a set of anti-blocking strands for the desired position at 37 °C for 40 min. The anti-blocking strands remove, by toehold-mediated strand displacement, the blocking strands at one of the predetermined docking sites on the rail, leaving that position available for the slider to attach. To release the slider back to the freely moving state, 50 nM of blocking strands for the currently attached position was added, and the sample incubated at 37 °C for 40 min.

For the non-interacting addresses in the one-pot system, 4 µL of bead-purified origami structure was mixed with 0.8 µL of 25 nM bridge strands to attach the slider to the desired position. The samples were then incubated for 1 h at room temperature. To release the slider back to a freely moving state, 0.4 µL of 5 µM release invaders was added, and the sample incubated for 1 h at room temperature.

Transmission Electron Microscopy (TEM): A FEI Tecnai T12 Transmission Electron Microscope (120kV) was used to characterize the origami structures and for analysis of attachment and stepping yield. Samples were prepared on glow-discharged (15 mA for 20 s) formvar-supported carbon-coated Cu300 TEM grids (Agar Scientific, Essex, UK). 10 µL of sample at 1 nM concentration was incubated on the grid for 2 min, blotted with paper, and negatively stained by a further 10 s incubation with 20 µL of 2% Uranyl Acetate (UA). Alternatively, a positive staining protocol was used where the UA step was followed by a 3 s spotting on a 20 µL drop of H_2O. After blotting, the grids were left to air dry for some minutes before imaging. Images were taken with a bottom-mounted 16 Megapixel Gatan OneView CMOS camera.

Images were analyzed using a custom Python script (Supporting Information). The path of the rail was traced manually by placing points, 20 pixels apart, along its track. The slider was marked at either end, its center point calculated and projected to the nearest point on the rail. The contour distances along the track to the two ends of the rail were calculated. For devices with sliders in an unbound state, the results presented correspond to the distance to the nearest end of the rail. For devices locked into position, measurements are displayed consistently from the same end of the rail: the authors plotted whichever of the two contour distances was closest to the designed docking position. Numbers of devices counted in each experiment are found in Table S4, Supporting Information.

DNA–PAINT Microscopy: The DNA–PAINT imaging was done in a Nanoimager S microscope (ONI, Oxford, UK) with a 532 nm laser in Total Internal Reflection Fluorescence mode. Exposures were 7000 frames of 300 ms. Post-processing was performed with Picasso.[44]

Samples were immobilized in channels formed with Ibidi sticky-slides VI 0.4 (Ibidi, Munich, Germany) with an oven-baked #1.5 glass coverslip as the bottom surface. Channels were incubated twice with 40 µL biotin-BSA solution (1 mg mL^{-1} BSA–biotin in Buffer A+ (10 mM Tris-HCl, 100 mM NaCl, and 0.05% vol/vol Tween 20 at pH 8.0)) for 2 min, followed by washes with 180 µL of buffer A+. Channels were then incubated with 40 µL streptavidin solution (0.5 mg ml^{-1} streptavidin in Buffer A+) for 2 min and washed again with Buffer A+. Channels were then incubated with a suspension of 60 nm gold nanoparticles (in Buffer A+) for 2 min, washed with 180 µL of Buffer A+, and washed with 180 µL Buffer B+ (5 mM Tris-HCl, 10 mM MgCl2, 1 mM EDTA, and 0.05% (vol/vol) Tween 20 at pH 8.0). The DNA origami sample diluted to around 0.1 nM in buffer B+ was then added and incubated for 2 min. Finally, the channel was washed with 180 µL of buffer B+ to remove unbound sample. Imager strands P1-Cy3 (CTAGATGTAT-Cy3) and P2-Cy3 (TATGTAGATC-Cy3) were diluted to 5 nM in buffer B+. First, 100 µL of P1 imager solution and the sample was imaged as above. The channel was then washed twice with 180 µL of buffer B+ before adding 100 µL of P2 imager solution, and re-imaged.

Supporting Information

Supporting Information is available from the Wiley Online Library or from the author.

Acknowledgements

E.B. and R.C.M. contributed equally to this work. This material is based upon work supported by the U.S. Department of Energy's Office of Energy Efficiency and Renewable Energy (EERE) under the Advanced Manufacturing Office Award Number DE-EE0008310. E.B. is supported by a Marie Skłodowska-Curie Individual Fellowship (grant agreement no. 842291). R.C.M. is supported by the European Union's Horizon 2020 research and innovation programme through the Marie Skłodowska-Curie "DNA Robotics" Innovative Training Network (grant agreement no. 765703). The authors thank William Shih (Wyss Institute, Harvard University) and Luzia Kilwing (Ludwig Maximilians University, Munich) for helpful discussions.

Conflict of Interest

The authors declare no conflict of interest.

Data Availability Statement

Research data are not shared.

Keywords

DNA origami, DNA nanotechnology, linear actuators, DNA mechanisms, self-assembly

Received: December 7, 2020
Revised: February 22, 2021
Published online: May 4, 2021

[1] N. C. Seeman, *J. Theor. Biol.* **1982**, *99*, 237.
[2] N. C. Seeman, H. F. Sleiman, *Nat. Rev. Mater.* **2018**, *3*, 17068.
[3] R. M. Dirks, N. A. Pierce, *Proc. Natl. Acad. Sci. U.S.A.* **2004**, *101*, 15275.
[4] L. Qian, E. Winfree, *Science* **2011**, *332*, 1196.
[5] S. M. Douglas, I. Bachelet, G. M. Church, *Science* **2012**, *335*, 831.
[6] E. S. Andersen, M. Dong, M. M. Nielsen, K. Jahn, R. Subramani, W. Mamdouh, M. M. Golas, B. Sander, H. Stark, C. L. P. Oliveira, J. S. Pedersen, V. Birkedal, F. Besenbacher, K. V. Gothelf, J. Kjems, *Nature* **2009**, *459*, 73.
[7] J. Shin, N. A. Pierce, *J. Am. Chem. Soc.* **2004**, *126*, 10834.
[8] S. J. Green, J. Bath, A. J. Turberfield, *Phys. Rev. Lett.* **2008**, *101*, 238101.
[9] R. P. Goodman, M. Heilemann, S. Doose, C. M. Erben, A. N. Kapanidis, A. J. Turberfield, *Nat. Nanotechnol.* **2008**, *3*, 93.
[10] Y. He, D. R. Liu, *Nat. Nanotechnol.* **2010**, *5*, 778.
[11] W. Meng, R. A. Muscat, M. L. Mckee, P. J. Milnes, A. H. El-sagheer, J. Bath, B. G. Davis, T. Brown, R. K. O. Reilly, A. J. Turberfiel, *Nat. Chem.* **2016**, *8*, 542.
[12] P. W. K. Rothemund, *Nature* **2006**, *440*, 297.
[13] S. M. Douglas, H. Dietz, T. Liedl, B. Högberg, F. Graf, W. M. Shih, *Nature* **2009**, *459*, 414.
[14] J. J. Funke, P. Ketterer, C. Lieleg, S. Schunter, P. Korber, H. Dietz, *Sci. Adv.* **2016**, *2*, e1600974.
[15] P. C. Nickels, B. Wünsch, P. Holzmeister, W. Bae, L. M. Kneer, D. Grohmann, P. Tinnefeld, T. Liedl, *Science* **2016**, *354*, 305.
[16] N. D. Derr, B. S. Goodman, R. Jungmann, A. E. Leschziner, W. M. Shih, S. L. Reck-Peterson, *Science* **2012**, *338*, 662.
[17] H. Gu, W. Yang, N. C. Seeman, *J. Am. Chem. Soc.* **2010**, *132*, 4352.
[18] Y. Zhao, A. Shaw, X. Zeng, E. Benson, A. M. Nyström, B. Högberg, *ACS Nano* **2012**, *6*, 8684.
[19] Q. Jiang, C. Song, J. Nangreave, X. Liu, L. Lin, D. Qiu, Z.-G. Wang, G. Zou, X. Liang, H. Yan, B. Ding, *J. Am. Chem. Soc.* **2012**, *134*, 13396.
[20] H. Gu, J. Chao, S.-J. Xiao, N. C. Seeman, *Nature* **2010**, *465*, 202.
[21] W. Sun, E. Boulais, Y. Hakobyan, W. L. Wang, A. Guan, M. Bathe, P. Yin, *Science* **2014**, *346*, 1258361.
[22] S. Helmi, C. Ziegler, D. J. Kauert, R. Seidel, *Nano Lett.* **2014**, *14*, 6693.
[23] A. Kuzyk, R. Schreiber, Z. Fan, G. Pardatscher, E.-M. Roller, A. Högele, F. C. Simmel, A. O. Govorov, T. Liedl, *Nature* **2012**, *483*, 311.
[24] H. T. Maune, S.-P. Han, R. D. Barish, M. Bockrath, W. a G. Iii, P. W. K. Rothemund, E. Winfree, *Nat. Nanotechnol.* **2010**, *5*, 61.
[25] G. Grossi, M. D. E. Jepsen, J. Kjems, E. S. Andersen, *Nat. Commun.* **2017**, *8*, 992.
[26] E. Kopperger, J. List, S. Madhira, F. Rothfischer, D. C. Lamb, F. C. Simmel, *Science* **2018**, *359*, 296.
[27] P. Ketterer, E. M. Willner, H. Dietz, *Sci. Adv.* **2016**, *2*, e1501209.
[28] S. Lauback, K. R. Mattioli, A. E. Marras, M. Armstrong, T. P. Rudibaugh, R. Sooryakumar, C. E. Castro, *Nat. Commun.* **2018**, *9*, 1446.
[29] A. E. Marras, L. Zhou, H.-J. Su, C. E. Castro, *Proc. Natl. Acad. Sci. U.S.A.* **2015**, *112*, 713.
[30] J. List, E. Falgenhauer, E. Kopperger, G. Pardatscher, F. C. Simmel, *Nat. Commun.* **2016**, *7*, 12414.
[31] J. T. Powell, B. O. Akhuetie-oni, Z. Zhang, C. Lin, *Angew. Chem., Int. Ed.* **2016**, *55*, 11412.
[32] D. Ackermann, T. L. Schmidt, J. S. Hannam, C. S. Purohit, A. Heckel, M. Famulok, *Nat. Nanotechnol.* **2010**, *5*, 436.
[33] T. Li, F. Lohmann, M. Famulok, *Nat. Commun.* **2014**, *5*, 4940.
[34] F. Lohmann, D. Ackermann, M. Famulok, *J. Am. Chem. Soc.* **2012**, *134*, 11884.
[35] M. Centola, J. Valero, M. Famulok, *J. Am. Chem. Soc.* **2017**, *139*, 16044.
[36] F. A. S. Engelhardt, F. Praetorius, C. H. Wachauf, G. Brüggenthies, F. Kohler, B. Kick, K. L. Kadletz, P. N. Pham, K. L. Behler, T. Gerling, H. Dietz, *ACS Nano* **2019**, *13*, 5015.
[37] Q. Xiong, C. Xie, Z. Zhang, L. Liu, J. T. Powell, Q. Shen, C. Lin, *Angew. Chem., Int. Ed.* **2020**, *59*, 3956.
[38] S. Brown, J. Majikes, H. Fennell, E. C. Samano, T. H. Labean, *Nanoscale* **2015**, *7*, 16621.
[39] T. Liedl, B. Högberg, J. Tytell, D. E. Ingber, W. M. Shih, *Nat. Nanotechnol.* **2010**, *5*, 520.
[40] D. J. Kauert, T. Kurth, T. Liedl, R. Seidel, *Nano Lett.* **2011**, *11*, 5558.
[41] C. E. Castro, H.-J. Su, A. E. Marras, L. Zhou, J. Johnson, *Nanoscale* **2015**, *7*, 5913.
[42] B. E. K. Snodin, J. S. Schreck, F. Romano, A. A. Louis, J. P. K. Doye, *Nucleic Acids Res.* **2019**, *47*, 1585.
[43] A. Shaw, E. Benson, B. Högberg, *ACS Nano* **2015**, *9*, 4968.
[44] J. Schnitzbauer, M. T. Strauss, T. Schlichthaerle, F. Schueder, R. Jungmann, *Nat. Protoc.* **2017**, *12*, 1198.
[45] R. Jungmann, M. S. Avendaño, J. B. Woehrstein, M. Dai, W. M. Shih, P. Yin, *Nat. Methods* **2014**, *11*, 313.
[46] W. B. Sherman, N. C. Seeman, *Nano Lett.* **2004**, *4*, 1203.
[47] S. M. Douglas, A. H. Marblestone, S. Teerapittayanon, A. Vazquez, G. M. Church, W. M. Shih, *Nucleic Acids Res.* **2009**, *37*, 5001.
[48] A. Suma, E. Poppleton, M. Matthies, Š. Petr, F. Romano, A. A. Louis, J. P. K. Doye, C. Micheletti, L. Rovigatti, *J. Comput. Chem.* **2019**, *40*, 2586.
[49] E. Poppleton, J. Bohlin, M. Matthies, S. Sharma, F. Zhang, P. Sulc, *Nucleic Acids Res.* **2020**, *48*, e72.
[50] J. Vieira, M. Joachim, *Methods Enzymol.* **1987**, *153*, 3.